

Incoherent elastic-neutron-scattering study of the vibrational dynamics and spin-related symmetry of protons in the KHCO_3 crystal

S. Ikeda

National Laboratory for High Energy Physics, Oho 1-1, Tsukuba, Ibaraki 305, Japan

F. Fillaux*

Laboratoire de Spectrochimie Infrarouge et Raman, CNRS, 2 rue Henry-Dunant, 94320 Thiais, France

(Received 4 August 1997; revised manuscript received 2 March 1998)

The potassium hydrogen carbonate crystal (KHCO_3) and its deuterated analog (KDCO_3) contain centrosymmetric dimer entities (HCO_3^-)₂, or (DCO_3^-)₂, linked by moderately strong hydrogen or deuterium bonds. The OH/OD bonds are virtually parallel to each other throughout the crystal. The incoherent elastic-neutron-scattering functions (IENSF) $S(Q_x, Q_y, Q_z=0, \omega=0)$ and $S(Q_x, Q_y=0, Q_z, \omega=0)$ were measured over the momentum transfer range from ~ 0 to $\sim 30 \text{ \AA}^{-1}$, with resolution of $\Delta|\mathbf{Q}| \sim 1 \text{ \AA}^{-1}$. The components of the momentum transfer Q_x , Q_y , and Q_z were parallel to the mean directions of the stretching, in-plane, and out-of-plane bending modes of protons or deuterons, respectively. For KHCO_3 , the broad incoherent scattering peaks, centered at $\mathbf{Q}=0$, are not amenable to the IENSF calculated with various models: the single harmonic oscillator, the double minimum potential, and the pair of coupled harmonic oscillators. Then, the degenerate ground state of a pair of coupled protons is regarded as composed of indistinguishable fermions. According to the Pauli principle, the symmetric and antisymmetric coordinates are singlet and triplet states, respectively. The IENSF gives quantum interferences that compare favorably to the observations. The estimated mean-square amplitudes in the ground state are amenable to isolated harmonic proton oscillators. Incoherent scattering for KDCO_3 is amenable to Gaussian profiles for bosons. There is no evidence for quantum interference. The profile narrowing reveals an increase of the mean-square amplitudes attributed to a rather large coupling of the deuteron dynamics to the crystal lattice. [S0163-1829(99)03305-6]

I. INTRODUCTION

Nowadays, incoherent inelastic-neutron-scattering (INS) spectra, obtained over a rather large energy transfer range (e.g., from ~ 0 to 4000 cm^{-1} with the TFXA spectrometer at the ISIS pulsed neutron source, Rutherford Appleton Laboratory, UK), provide information on the vibrational dynamics in solids that cannot be obtained with the optical techniques (infrared and Raman). Although the INS technique is rather young, it has already had a spectacular impact on two central problems of vibrational spectroscopy: the relevance of normal modes to represent vibrational spectra and the quantum transfer of protons within double minimum potential wells.¹

A. Normal versus localized modes

It is widely accepted that vibrational dynamics of atoms and molecules are reasonably well represented with normal coordinates.² Unfortunately, band intensities measured with the optical techniques cannot be fully exploited, and force fields refined with respect to the observed frequencies only are largely underdetermined.

With the INS technique, force fields can be refined with respect to the full spectral profiles including both frequencies and intensities.³⁻⁹ The incoherent scattering cross section for protons being about one order of magnitude greater than for any other atom, this INS technique is most powerful for hydrogenous samples.

When harmonic force fields are used to represent local atom-atom interactions in molecular crystals, the mean posi-

tions of the protons that oscillate at high frequency (internal modes) follow adiabatically the slow lattice vibrations corresponding to translational and librational motions of the heavy molecular entities, usually referred to as external modes in this context. This riding effect should give rise to large intensities for the lattice modes at low frequency and the intensities of the internal molecular vibrations should be depressed dramatically by the Debye-Waller factor.⁸ Consequently, it has been speculated that internal modes above $\sim 1000 \text{ cm}^{-1}$ should be almost invisible with INS. However, this is largely in error. For example, CH stretching modes were observed at $\sim 3000 \text{ cm}^{-1}$ and the role of the Debye-Waller factor had to be reconsidered.⁴⁻⁷

More recently, it has been shown that the INS spectrum of potassium hydrogen carbonate (KHCO_3) cannot be represented with conventional harmonic force fields.¹⁰ The observed lattice-mode intensity is far too weak. The proton dynamics almost totally decoupled from the heavy atoms are better represented with localized modes in a "fixed" (laboratory) referential frame. From the standpoint of the INS spectrum, KHCO_3 can be regarded as a crystal of protons so weakly coupled to the surrounding atoms that the framework of carbonate and K^+ ions can be virtually ignored. Dynamical models are thus greatly simplified. This view is not specific to the ionic nature of the crystal.^{11,12}

These results severely undermine the representation of vibrational spectra with usual normal modes. However, the phenomenological approach proposed so far lacks of contact with physics. It has been recently speculated that the decoupling of the proton dynamics from the crystal lattice could be

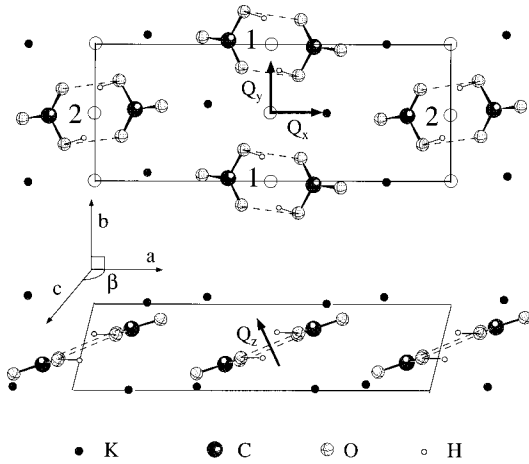


FIG. 1. Schematic view of the crystalline structure of KHCO_3 after Ref. 22.

a consequence of the spin correlation for indistinguishable fermions, according to the Pauli principle.¹³ Then, incoherent elastic-neutron-scattering (IENS) measurements of KHCO_3 should reveal quantum interferences. As opposed to this, quantum interferences should not be observed for KDCO_3 (bosons) and the deuteron dynamics could be coupled to the lattice.

B. Proton transfer

The proton transfer along pre-existing hydrogen bonds is one of the simplest chemical reactions which is of great importance in many fields in physics, chemistry, and biology.^{14–19} KHCO_3 is a prototypical system for proton transfer dynamics^{10,20,21} because the crystal contains centrosymmetric dimer entities $(\text{HCO}_3^-)_2$ (Fig. 1), and this structure remains unchanged from 298 to 98 K.^{22,23} (We are not aware of any diffraction work at a lower temperature). The hydrogen bond with length $\text{O}\cdots\text{O}=2.587 \text{ \AA}$ (2.607 \AA for KDCO_3) is moderately strong.²⁴ At 298 K protons are disordered between two sites located at $\sim \pm 0.3 \text{ \AA}$ off-center of the hydrogen bond, with population ratio of $\sim 1:4$.

Tunneling for proton transfer is best observed for the stretching vibration along the reaction path. In the infrared and Raman this mode gives broad bands, with several submaxima between 1800 and 3500 cm^{-1} ,^{25–27} amenable to a quasisymmetric double minimum potential.²⁰ The “tunneling” transition for the quantum transfer of a single proton was observed at 216 cm^{-1} with the INS technique.¹⁰ (There is no evidence for double minimum potential along the bending modes.) Surprisingly, the “tunneling” band is rather sharp. On the one hand, this confirms that the proton transfer is largely decoupled from the heavy atom dynamics, in line with the remainder of the spectrum. On the other hand, this is in contrast to the “phonon-assisted tunneling” model¹⁸ that supposes a large modulation of the double minimum potential by the $(\text{O}\cdots\text{O})$ low-frequency modes of the hydrogen bond. Tunneling transitions observed in various hydrogen bonds are quite similar.²⁸

C. The neutron-scattering function

For proton dynamics studies, INS spectra can be measured over a range of momentum transfer $\mathbf{Q}=\mathbf{k}_i-\mathbf{k}_f$ with

TABLE I. Thermal neutron-scattering cross sections in barns, according to Ref. 29.

	Spin	Coherent	Incoherent	Absorption
^1H	1/2	1.76	79.91	0.33
^2D	1	5.60	2.04	0.00
^{12}C	0	5.56	0	0.00
^{16}O	0	4.23	0	0.00
^{39}K	3/2	1.81	0.25	2.1

$|\mathbf{k}_i|=2\pi/\lambda_i$ and $|\mathbf{k}_f|=2\pi/\lambda_f$, where λ_i and λ_f are the incident and scattered wavelengths, respectively. Owing to the large incoherent scattering cross section for protons, compared to other atoms (see Table I), the scattered intensity can be represented with the incoherent neutron-scattering function (INSF)⁸

$$S(\mathbf{Q}, \omega) = |\langle \Psi_f(\mathbf{r}) | \exp(i\mathbf{Q}\cdot\mathbf{r}) | \Psi_i(\mathbf{r}) \rangle|^2 \delta(E_{if} - \hbar\omega), \quad (1)$$

where $\Psi_i(\mathbf{r})$ and $\Psi_f(\mathbf{r})$ are the wave functions, depending on the spatial coordinate \mathbf{r} , in the initial and final states, respectively. E_{if} is the energy of the transition and $\hbar\omega$ is the neutron energy transfer. The spectral profile in \mathbf{Q} contains spatial information on the wave functions.

The peculiar aspects of the proton dynamics in KHCO_3 presented above were derived from INS data collected with the TFXA spectrometer.¹⁰ For this instrument, momentum and energy transfers are correlated as $\hbar\omega \sim \hbar^2 Q^2 / 2m_n$, where m_n is the neutron mass. Therefore, important information on the proton dynamics is lacking.

With the MARI spectrometer at the ISIS pulsed neutron source, the INSF can be measured over the rather large $|\mathbf{Q}|$ range required for a complete representation of the proton dynamics (for example from ~ 0 to $\sim 30 \text{ \AA}^{-1}$ for elastic scattering with an incident energy of $\sim 500 \text{ meV}$). In this paper, only the incoherent elastic-neutron-scattering function (IENSF) is considered. The $S(\mathbf{Q}, \omega=0)$ provides a model independent view of the wave function in the ground state.

With single crystals, the IENSF $S(Q_x, Q_y, Q_z, \omega=0)$ can be measured for momentum transfer along specific directions. In the KHCO_3 (KDCO_3) crystal, $\text{OH}(\text{OD})$ bonds are virtually parallel to each other (see Fig. 1) and Q_x , Q_y and Q_z were chosen parallel to the mean directions of the proton or deuteron modes: stretching (ν OH/OD), in-plane bending (δ OH/OD) and out-of-plane bending (γ OH/OD), respectively. Two slices of the IENSF in the (Q_x, Q_y) and (Q_x, Q_z) planes for KHCO_3 (Figs. 2 and 3) and one slice in the (Q_x, Q_z) plane for KDCO_3 (Fig. 4) were obtained (for experimental details see Sec. II).

Both coherent (diffraction) and incoherent scattering contribute to the maps of intensity. For KHCO_3 incoherent scattering by protons gives a broad peak centered at $\mathbf{Q}=0$. There is no incoherent scattering by C and O atoms and the contribution of K atoms is negligible (Table I). In order to optimize the signal-to-noise ratio we have symmetrized the maps of intensity. For $S(Q_x, Q_y, 0)$ this is straightforward since the reciprocal lattice is orthogonal. The reciprocal lattice for $S(Q_x, Q_z, 0)$, on the other hand, is not orthogonal and unfolding the map introduces symmetry elements that do not

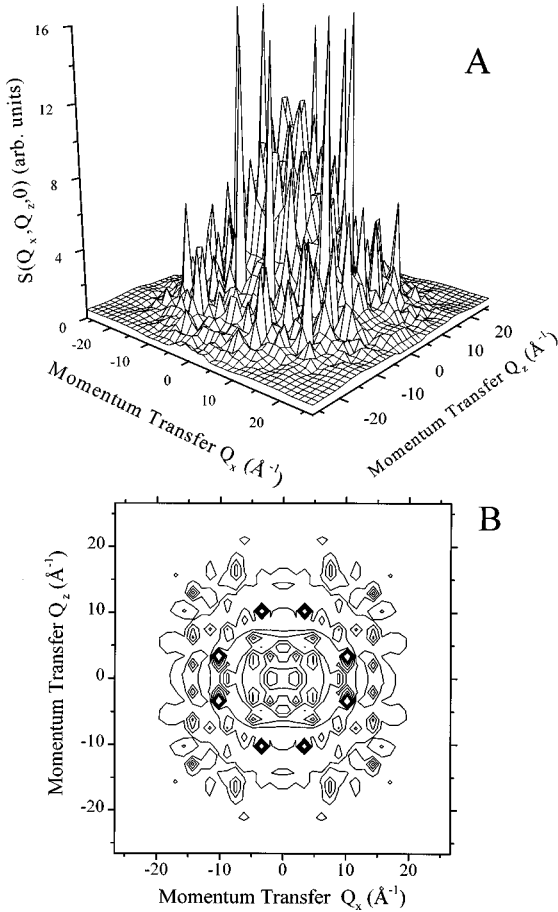


FIG. 2. KHCO_3 : $S(Q_x, Q_y, 0)$ with Q_x and Q_y parallel to the dimer planes, along the a and b crystal axes, respectively. Intensities were integrated over $-10 \text{ cm}^{-1} < \hbar\omega < 10 \text{ cm}^{-1}$. (A) landscape view; (B) isointensity contour map.

exist in the crystal. This is of negligible impact for the analysis of diffuse incoherent scattering.

Coherent scattering gives Bragg peaks. However, the MARI spectrometer is not suited to diffraction measurements. The pixel size determined by the experimental resolution in $|\mathbf{Q}|$ ($\sim 1 \text{ \AA}^{-1}$) is comparable to the size of the unit cell in the reciprocal plane (Q_x, Q_y) and much larger in (Q_x, Q_z). Consequently, most of the Bragg peaks are not resolved and give a smoothed background intensity proportional to the coherent scattering cross section. For KHCO_3 , this background is negligible. However, sharp peaks are observed at rather large momentum transfer values ($|\mathbf{Q}| > 10 \text{ \AA}^{-1}$), far beyond the \mathbf{Q} range measured in previous diffraction works.^{22,23} Unfortunately, it is not possible to index these peaks unambiguously. In addition, regarding the rather large crystal size, multiple coherent scattering events cannot be excluded. Therefore, these peaks are not discussed any further in this paper. The data analysis and discussion presented below are focused on the IENS profiles. For KDCO_3 , the incoherent scattering cross section of the D atom is rather weak and coherent scattering is most important (see Table I).

D. The proton dynamics

For KHCO_3 , the isointensity contours (Figs. 2 and 3) and cuts along the vibrational modes are quite different from the

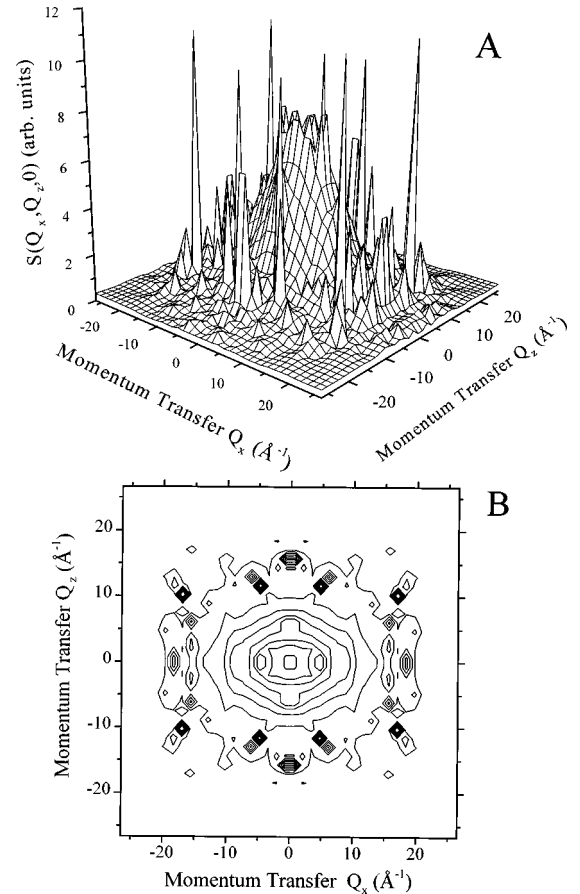


FIG. 3. KHCO_3 : $S(Q_x, Q_z, 0)$ with Q_x parallel to the long dimer axis and Q_z perpendicular to the dimer plane. Intensities were integrated over $-10 \text{ cm}^{-1} < \hbar\omega < 10 \text{ cm}^{-1}$. (A) landscape view; (B) isointensity contour map.

shapes anticipated for harmonic oscillators, or double minimum potentials or pairs of coupled oscillators (see Secs. IV A, B, C, below). The IENSF calculated for pairs of coupled fermions with spin correlation¹³ compares favorably to the observation (see Sec. IV D, below). The major output of this analysis is that quantum interferences are likely. In addition, the estimated mean-square amplitudes for proton modes (see Table II) correspond to well-isolated harmonic oscillators, and this conclusion is model independent.

For the deuterated analog (see Fig. 4) cuts along Q_x and Q_z are amenable to the Gaussian profiles for harmonic oscillators. There is no evidence for quantum interferences. In addition, the profiles are much narrower than anticipated if the deuterons (like protons) were amenable to isolated harmonic oscillators. It is concluded that the deuteron dynamics are largely coupled to the lattice.

II. EXPERIMENT

A. Crystal structure and symmetry

The KHCO_3 crystal is monoclinic, space group $P2_1/a(C_{2h}^5)$, with four KHCO_3 entities per unit cell ($a = 15.1725 \text{ \AA}$, $b = 5.6283 \text{ \AA}$, $c = 3.7110 \text{ \AA}$, $\beta = 104.631^\circ$).²² The centrosymmetric dimers $(\text{HCO}_3^-)_2$, oc-

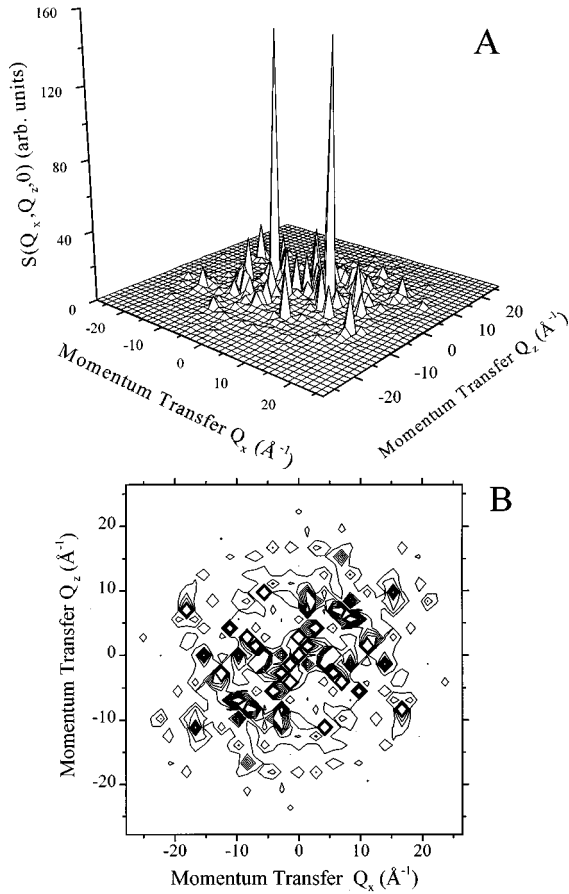


FIG. 4. KDCO₃: $S(Q_x, Q_z, 0)$ with Q_x parallel to the long dimer axis and Q_z perpendicular to the dimer plane. Intensities were integrated over $-10 \text{ cm}^{-1} < \hbar\omega < 10 \text{ cm}^{-1}$. (A) landscape view; (B) isointensity contour map.

copy C_i sites. They are parallel to the (103) planes at 14° with respect to the (a, b) planes.

Two single crystals of KHCO₃ with cylindrical shapes (diameter ~ 1 cm, length ~ 3 cm) were studied. The cylinder axes were oriented either perpendicular to the dimer planes (sample I) or parallel to the projections of the b crystal axis onto the (103) planes (samples II). The single crystal of KDCO₃ (sample IID with $D/H > 99.9\%$) was analogous to sample II.

B. Spectra

The MARI spectrometer at the ISIS pulsed neutron source is a direct geometry spectrometer. The detectors continuously cover all the angles from 3° to 135° , all with the same length of secondary flight path (~ 4 m). For each sample, dimer planes were either parallel or perpendicular to the plane containing the detector bank and the incident beam. The incident energy was $E_i \sim 500$ meV ($\lambda_i \sim 0.4 \text{ \AA}$) with resolution of $\Delta E_i/E_i \sim 2\%$.

Measurements were carried out in such a way that the momentum transfer was either parallel or perpendicular to the mean dimer plane. The cylinder axis (Z) of the crystal was oriented perpendicular to the (X, Y) plane containing the detector bank (Fig. 5) and the X axis is parallel to the incident wave vector (\mathbf{k}_0). Only neutrons scattered almost par-

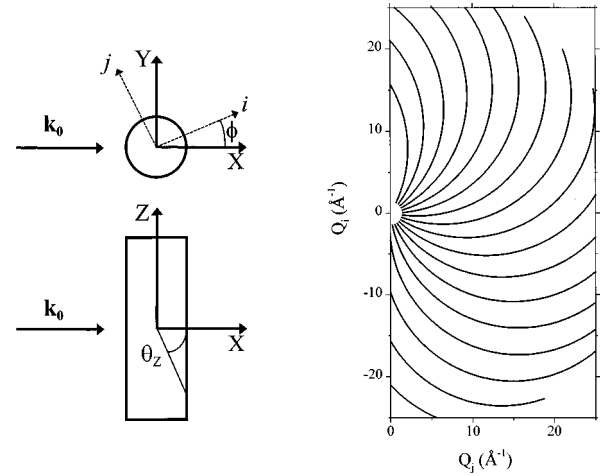


FIG. 5. Left: schematic representation of the sample orientation. The diameter is 1 cm and the length 3 cm. \mathbf{k}_0 is the incident wave vector ($|\mathbf{k}_0| \sim 15.7 \text{ \AA}^{-1}$). The detector bank and the crystal axes i and j are in the (X, Y) plane. Right: elastic scans in the (Q_i, Q_j) plane for various crystal orientations (ϕ).

allel to the (X, Y) plane ($Q_z \sim 0$) illuminate the detectors and, in the measurements under consideration, only those neutrons whose final energy is equal to the incident energy are selected ($\hbar\omega \sim 0$).

The orientation of the crystal with respect to the incident beam (ϕ) was rotated from 0 to 180° , by steps of 12° , in order to probe a half plane in reciprocal space (see Fig. 5). Data were converted from counts per channel per angle to $S(Q_i, Q_j, \omega)$ with standard procedures. In order to minimize the contribution of inelastic scattering, the maps of intensity were obtained after integration from -10 to 10 cm^{-1} .

C. Multiple scattering

Using standard values, the incoherent cross section per cm^3 of KHCO₃ is $\Sigma_{\text{inc}}(H) \sim 1 \text{ cm}^{-1}$. Absorption is negligible. The neutron mean free path (~ 1 cm) is on the order of the crystal size and the probability of measuring multiple-scattering events must be estimated. In order to minimize these effects, we take advantage of the MARI spectrometer geometry and of the shape of the sample.

Using the averaged sample size along X ($4R/\pi \sim 0.64$ cm), the neutron transmission is ~ 0.55 . The probability for a first scattering event is $P_1 \sim 0.45$. With an incident energy of 500 meV, incoherent scattering for the $0 \rightarrow 0$, $0 \rightarrow 1$, and $0 \rightarrow 2$ transitions between proton states can occur with probabilities ~ 0.53 , 0.27 , and 0.20 , respectively. Therefore, elastic scattering occurs for $\sim 24\%$ and inelastic scattering for $\sim 21\%$ of the incident neutron flux in the sample (Φ_0). This is a rough estimation that does not account for the real density of states. The aperture of the detector bank along the Z axis is $\sim 14^\circ$. Consequently, $\sim 25\%$ of the neutrons undergoing elastic scattering ($\sim 6\%$ of Φ_0) have $|Q_z|$ values required to reach the detectors ($|Q_z| < 2 \text{ \AA}^{-1}$).

For a hydrogenated sample at low temperature, the energy constraints ($\hbar\omega_1 + \hbar\omega_2 \sim 0$ and $\hbar\omega_1 \gg kT$) eliminate most of neutrons undergoing inelastic scattering from the measurements. Practically, only multiple elastic-scattering events

must be considered. The averaged location in the (X, Y) plane of the first scattering event is at the center of the sample. The mean path length for those neutrons which have been scattered once is virtually independent of Q_X and Q_Y . For $Q_Z = 2k_0 \sin(\theta_Z/2)$ the mean path length is $R/\cos\theta_Z$, for $\theta_Z \leq 70^\circ$, and $1.5R$ for $70^\circ \leq \theta_Z \leq 90^\circ$, with $R \sim 0.5$ cm (see Fig. 5). Numerical calculations of the transmission factor $T(Q_Z) = \exp\{-\sum_{\text{inc}}(H)R/\cos[2 \arcsin(Q_Z/2k_0)]\}$ confirm that the mean transmission factor is very similar to the transmission for the mean path length.

The probability $p_2(Q_Z)$ for double incoherent elastic-scattering events with successive momentum transfers Q_Z and $-Q_Z$ is proportional to the square of the normalized scattering law. Within the harmonic approximation,

$$p_2(Q_Z) \sim 0.24[1 - T(Q_Z)] \frac{u_{0Z}^2}{\pi} \exp(-2u_{0Z}^2 Q_Z^2)$$

decreases rapidly for large Q_Z values. With $u_{0Z}^2 = 0.01 \text{ \AA}^2$, $P_{Z2} = \int p_2(Q_Z) dQ_Z \sim 0.0017$. This value is underestimated because the constraint for Q_Z is not strictly zero. With

$$\int_{-2}^2 \exp[-2u_{0Z}^2(Q_Z^2 - q_Z^2)] dq_Z \sim 4 \exp(-2u_{0Z}^2 Q_Z^2),$$

a probability of ~ 0.007 is more realistic. Compared to the probability for incoherent elastic-scattering events at small Q_Z values (~ 0.06), the contribution of double-scattering events is $\sim 10\%$ of the measured signal. The probability for more than two successive incoherent elastic-scattering events is negligible.

These calculations are only indicative. Nevertheless, they demonstrate that the spectrometer related constraint $Q_{Z1} + Q_{Z2} < 2 \text{ \AA}^{-1}$ cancels contributions of most multiple incoherent elastic-scattering events with nonzero momentum transfer along the Z axis. The main contribution to multiple scattering is due to those neutrons which have been scattered elastically twice with Q_{Z1} and $Q_{Z2} < 2 \text{ \AA}^{-1}$ ($\sim 6\%$ of the measured signal).

Multiple scattering of $\sim 10\%$ has little consequences on the measurements of incoherent scattering (see Fig. 6). The widths are changed by less than 1%. According to numerical simulations for 25% and 50% multiple scattering, the width are increased by $\sim 4\%$ and 10% , respectively. Therefore, multiple-scattering effects should be negligible, compared to other experimental errors. This is largely confirmed by the data analysis presented below. For KDCO_3 , multiple incoherent scattering events can be ignored. The situation is totally different for multiple coherent scattering which may give rise to Bragg-like peaks for both KHCO_3 and KDCO_3 .

III. PAIRS OF COUPLED OSCILLATORS: THEORY

In KHCO_3 , intra- and interdimer coupling terms can be distinguished with optical and INS techniques. The intradimer terms give band splitting into B_u and A_g symmetry species observed in the infrared and with Raman, respectively.²⁵⁻²⁷ The splitting is quite different for the three modes: ~ 200 , 60 , and 40 cm^{-1} for the stretching, in-plane, and out-of-plane bending, respectively. The INS technique, on the other hand, probes the density of states due to interdimer coupling terms. However, the observed bandwidths for

the proton modes are similar with the three techniques. Consequently, interdimer coupling terms can be neglected and the proton dynamics for each degree of freedom can be represented with two identical harmonic oscillators with mass m moving along collinear coordinates x_1 , x_2 , and coupled to one another. The Hamiltonian is³⁰

$$H = \frac{1}{2m} (P_1^2 + P_2^2) + \frac{1}{2} m \omega_{0x}^2 [(x_1 - x_0)^2 + (x_2 + x_0)^2 + 2\lambda_x (x_1 - x_2)^2]. \quad (2)$$

P_1 and P_2 are the kinetic momenta. The harmonic frequency of the uncoupled oscillators at equilibrium positions $\pm x_0$ is ω_{0x} . The coupling potential proportional to λ_x depends only on the distance between the pendula. The equilibrium positions of the coupled oscillators are at $\pm x'_0 = \pm x_0 / (1 + 4\lambda_x)$.

A. Normal coordinates

Normal coordinates are symmetric (x_s) and antisymmetric (x_a) displacements of the particles. For the sake of simplicity, it is convenient to use normalized coordinates corresponding to an effective mass of m for each mode

$$x_a = \frac{1}{\sqrt{2}} (x_1 + x_2), \quad P_a = \frac{1}{\sqrt{2}} (P_1 + P_2), \quad (3)$$

$$x_s = \frac{1}{\sqrt{2}} (x_1 - x_2), \quad P_s = \frac{1}{\sqrt{2}} (P_1 - P_2).$$

Substitution in Eq. (2) gives the desired separation of the normal modes

$$H = \left\{ \frac{P_a^2}{2m} + \frac{1}{2} m \omega_{0x}^2 x_a^2 \right\} + \left\{ \frac{P_s^2}{2m} + \frac{1}{2} m \omega_{0x}^2 (1 + 4\lambda_x) \right\} \times [x_s - \sqrt{2}x'_0]^2 + m \omega_{0x}^2 x_0^2 \frac{4\lambda_x}{1 + 4\lambda_x}. \quad (4)$$

The normal frequencies are then

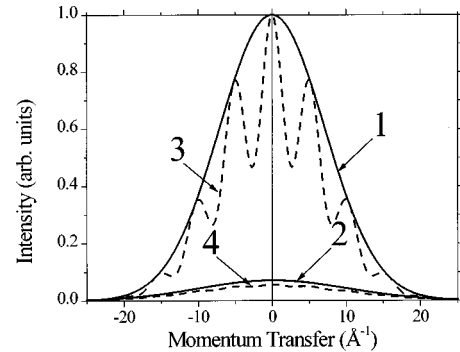


FIG. 6. Comparison of the incoherent profiles due to single and double elastic scattering events with probabilities 1 and 0.1, respectively. Solid lines: harmonic oscillator with $u_0^2 = 0.01 \text{ \AA}^2$. Dash lines: coupled fermion oscillators [according to Eq. (17)] with the same u_0^2 values and $x'_0 = 0.3 \text{ \AA}$. The profiles for double scattering (curves 2 and 4) are self-convolutions of the profiles for single scattering (curves 1 and 3, respectively).

$$\omega_a = \omega_{0x} \quad \text{and} \quad \omega_s = \omega_{0x} \sqrt{1 + 4\lambda_x}. \quad (5)$$

The quantization of the normal coordinates gives³⁰

$$\Psi_{a\sigma} = \Psi_\alpha^a(x_a) \times \Psi_\sigma^s(x_s - \sqrt{2}x'_0),$$

and

$$E_{a\sigma} = \left(\alpha + \frac{1}{2} \right) \hbar \omega_a + \left(\sigma + \frac{1}{2} \right) \hbar \omega_s. \quad (6)$$

B. Spin-related symmetry in the ground state

The wave function for the degenerate ground state in Eq. (6) is relevant only for bosons. For fermions, spins are correlated in such a way that the total wave function is antisymmetrical with respect to particle permutations, according to the Pauli principle. The spatial part of the wave function is symmetrical (Θ_{0+}) for the singlet state ($S=0$) and antisymmetrical (Θ_{0-}) for the triplet state ($S=1$)

$$\Theta_{0\pm}(x_1, x_2) = \frac{1}{\sqrt{2}} \Psi_0^a(x_a) [\Psi_0^s(x_s - \sqrt{2}x'_0) \pm \Psi_0^s(x_s + \sqrt{2}x'_0)]. \quad (7)$$

These wave functions apply to any pair of coupled protons, irrespective of the distance and of the magnitude of the coupling term, provided it is not zero. The Pauli principle imposes the symmetry of the wave function while the ground state remains degenerate. It is no longer possible to distinguish the spin operators for each nucleus. A pair of coupled protons must be regarded as a composed boson with spin $S=1$.

C. Vibrational coupling

In the KHCO_3 crystal, protons are engaged in hydrogen bonds between two carbonate entities (CO_3^{2-}) forming centrosymmetric dimers. If there is no coupling term between the protons and the dimer oscillations, the dynamics is represented with symmetric and antisymmetric normal coordinates for the proton modes (x_s, x_a) and for the dimer modes (say X_s, X_a). (For the sake of clarity, we consider only two sets of normal coordinates). In the boson case the wave function analogous to Eq. (6) is

$$\Xi_0(x_1, x_2, X_1, X_2) = \Psi_0^a(x_a) \Psi_0^s(x_s - \sqrt{2}x'_0) \Phi_0^a(X_a) \times \Phi_0^s(X_s - \sqrt{2}X'_0). \quad (8)$$

Here, the equilibrium positions for the dimer coordinates are at $\pm X'_0$.

Alternatively, if nuclear spins are taken into consideration, the wave function in the ground state is antisymmetrical with respect to proton permutation and it is invariant for permutation of the CO_3^{2-} entities, since carbon and oxygen atoms are bosons. The wave function analogous to Eq. (8) is

$$\Xi_{0\pm}(x_1, x_2, X_1, X_2) = \frac{1}{\sqrt{2}} \Psi_0^a(x_a) [\Psi_{s0}(x_s - \sqrt{2}x'_0) \pm \Psi_0^s(x_2 + \sqrt{2}x'_0)] \Phi_0^a(X_a) \times \Phi_0^s(X_s - \sqrt{2}X'_0). \quad (9)$$

If protons and dimers are coupled via nonzero off-diagonal elements in the dynamical matrix, fermions and bosons cannot be separated and it is not possible to define antisymmetrized wave functions analogous to Eq. (9). However, this is in conflict with the Pauli principle since the two protons are indistinguishable in the ground state. Therefore, the dynamics of a pair of indistinguishable (coupled) fermions must be uncorrelated (uncoupled) to the lattice dynamics.

For systems containing several sets of indistinguishable fermions, for instance $\text{KH}^{13}\text{C}^{17}\text{O}_3$, the wave function should be antisymmetrized with respect to permutations for each set of indistinguishable fermions (H, ^{13}C , and ^{17}O , respectively). Nonzero off-diagonal elements mixing different sets of indistinguishable fermions with each other or with boson coordinates are forbidden.

The factorization of the wave function may account for the localized proton modes introduced empirically on the basis of previous observations.¹⁰⁻¹² This decoupling, observed for different systems, is not likely due to accidental cancellation of off-diagonal elements. It could also account for the observation of well-defined bands at high energy and momentum transfer values in molecular crystals⁴⁻⁷ since the lattice modes should not contribute to the attenuation factor for the proton modes. Finally, the factorization of the wave function could be a limitation to the phonon-assisted tunneling model.¹⁷ However, large anharmonicity may also contribute to the separation of the dynamics of light and heavy particles.

The Pauli principle applies only to the degenerate ground state. The excited vibrational states have no degeneracy [see Eq. (6)] and the dynamics can be represented with usual normal modes including all atomic coordinates. Therefore, the normal coordinates could be different in the ground and excited states. In addition, force fields could be different for hydrogenated and deuterated analogs.

IV. SCATTERING FUNCTIONS: COMPARISON WITH EXPERIMENTS

In order to establish the specific manifestations of spin correlations, the IENSF for the harmonic oscillator, for the double minimum potential and for pairs of coupled oscillators composed of either bosons or fermions are calculated¹³ and compared to the observations. For each model, the observed profiles are decomposed into the IENSF profile and triangular functions corresponding to other scattering processes (for instance, Bragg reflections, see Figs. 7–14). The numerical values for the best fits given in Table II were obtained with a least-squares procedure allowing all parameters to be adjusted.

A. Harmonic potential

The IENSF is Gaussian in shape, centered at $Q_x=0$:

$$S(Q_x, \omega) = \exp(-Q_x^2 u_{0x}^2) \delta(\omega). \quad (10)$$

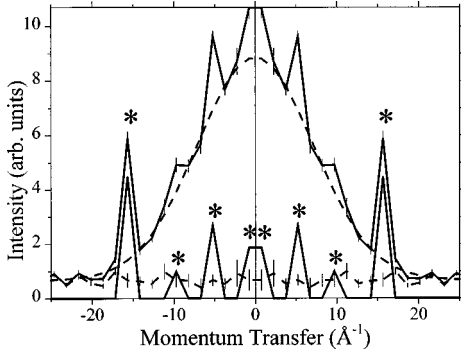


FIG. 7. KHCO_3 : cut of $S(Q_x, Q_y, 0)$ at $\pm 20^\circ$ with respect to Q_x . Comparison of the measured profile (solid line with error bars) to the best fit (dash line) obtained with a harmonic profile ($u_{0x}^2 = 0.99 \times 10^{-2} \text{ \AA}^2$, $\hbar \omega_{0x} = 1690 \text{ cm}^{-1}$) and eight triangular functions (solid line and *) attributed to other scattering processes. The dash line with error bars is the difference spectrum.

The mean-square amplitude

$$u_{0x}^2 = \langle \Psi_0(x) | x^2 | \Psi_0(x) \rangle = \frac{\hbar}{2m\omega_{0x}}. \quad (11)$$

The best fits to cuts of $S(Q_x, Q_y, 0)$ along the ν OH and δ OH modes (Figs. 7 and 8) give mean-square amplitudes (see Table II) close to those anticipated for the very anharmonic potential of the stretching mode^{10,20,21} and for the almost harmonic potential of the in-plane bending mode. Similar results were obtained for cuts of $S(Q_x, Q_z, 0)$ (see Table II). However, it is necessary to include a rather large number of triangular functions.

B. Double minimum potential

For a single particle in a symmetrical double minimum potential the ground state splits into two sublevels, symmetric (0^+) and antisymmetric (0^-), respectively. $E_{0^-} - E_{0^+} = \hbar \omega_{0-}$ is the tunnel splitting. If the potential barrier is sufficiently high, convenient approximations of the wave functions are symmetrical and antisymmetrical combinations of harmonic wave functions centered at the potential minima $\pm x_0$

$$\Psi_{0\pm}(x) = \frac{1}{\sqrt{2[1 \pm \exp(-x_0^2/2u_{0x}^2)]}} [\Psi_0(x - x_0) \pm \Psi_0(x + x_0)]. \quad (12)$$

TABLE II. Estimated mean-square amplitudes u_0^2 and $\hbar \omega_0$ (cm^{-1}) = $16.759/u^2$ (\AA^2) along Q_x (ν OH/OD), Q_y (δ OH) and Q_z (γ OH/OD) in the (Q_x, Q_y) and (Q_x, Q_z) planes. Best fits were obtained with the harmonic model, Eq. (10), and with Eq. (17) for quantum interferences. In this latter case, r_0 is the half-distance between two correlated protons.

Map	Q	KHCO_3		KDCO_3			
		Harmonic		Quantum interferences		Harmonic	
		u_0^2 (10^{-2} \AA^2)	$\hbar \omega_0$ (cm^{-1})	u_0^2 (10^{-2} \AA^2)	$\hbar \omega_0$ (cm^{-1})	r_0 (\AA)	u_0^2 (10^{-2} \AA^2)
$S(Q_x, Q_y, 0)$	Q_x	0.99 ± 0.05	1690 ± 60	0.94 ± 0.02	1780 ± 40	0.31 ± 0.02	
	Q_y	1.25 ± 0.05	1340 ± 50	1.26 ± 0.02	1325 ± 30	0.31 ± 0.02	
$S(Q_x, Q_z, 0)$	Q_x	0.79 ± 0.05	2110 ± 80	0.84 ± 0.02	2000 ± 50	0.33 ± 0.02	0.91 ± 0.05
	Q_z	1.29 ± 0.05	1300 ± 50	1.36 ± 0.02	1230 ± 20	0.25 ± 0.02	2.31 ± 0.05

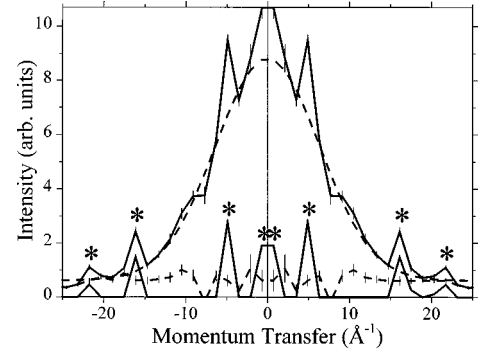


FIG. 8. KHCO_3 : cut of $S(Q_x, Q_y, 0)$ along Q_y . Comparison of the measured profile (solid line with error bars) to the best fit (dash line) obtained with a harmonic profile ($u_{0y}^2 = 1.25 \times 10^{-2} \text{ \AA}^2$, $\hbar \omega_{0y} = 1340 \text{ cm}^{-1}$) and eight triangular functions (solid line and *) attributed to other scattering processes. The dash line with error bars is the difference spectrum.

The scattering functions are

$$S(Q_x, \omega)_{0+0+} = \frac{1}{1 + \exp(-x_0^2/2u_{0x}^2)} \times \left[\cos(Q_x x_0) + \exp\left(-\frac{x_0^2}{2u_{0x}^2}\right) \right] \times \exp\left(-\frac{Q_x^2 u_{0x}^2}{2}\right) \delta(\omega),$$

$$S(Q_x, \omega)_{0+0-} = S(Q_x, \omega)_{0-0+} = \frac{1}{\sqrt{1 - \exp(-x_0^2/u_{0x}^2)}} \left| i \sin(Q_x x_0) \right| \times \exp\left(-\frac{Q_x^2 u_{0x}^2}{2}\right) \delta(\omega_0 \pm \omega), \quad (13)$$

$$S(Q_x, \omega)_{0-0-} = \frac{1}{1 - \exp(-x_0^2/2u_{0x}^2)} \times \left[\cos(Q_x x_0) - \exp\left(-\frac{x_0^2}{2u_{0x}^2}\right) \right] \times \exp\left(-\frac{Q_x^2 u_{0x}^2}{2}\right) \delta(\omega).$$

The periodical terms account for the interference between neutrons scattered by protons delocalized over the two sites. For elastic scattering, S_{0+0+} and S_{0-0-} give an interference pattern analogous to the optical fringes for two slits separated by $2x_0$ whose widths are u_{0x}^2 . The intensity is a maximum at $Q_x x_0 = n\pi$. It can be observed only with sufficient energy resolution. Otherwise, the interference pattern due to S_{0+0-} and S_{0-0+} , which correspond to inelastic scattering at $\pm \hbar \omega_{0-}$, is measured simultaneously. Then, the summation of $\sin^2(Q_x x_0)$ and $\cos^2(Q_x x_0)$ factors in Eq. (13) gives a spectrum very similar to, and practically indistinguishable from that of a harmonic oscillator. Very similar conclusions apply to quasimmetrical double minimum potentials.

The cut along the stretching mode direction (Fig. 7) reveals secondary maxima of intensity at $\sim \pm 5 \text{ \AA}^{-1}$. If they were due to proton tunneling, the distance between the two potential minima should be $2x_0 \sim 1.2 \text{ \AA}$. This is about twice the distance consistent with the crystal structure and with the asymmetrical double minimum potential function previously proposed for the stretching coordinate.¹⁰ In addition, similar profiles are observed for cuts along the bending modes (for example, see Fig. 8), whereas the potential is single minimum. Therefore, the observed profiles cannot be attributed to proton tunneling.

C. Pair of coupled bosons

With the wave function given in Eq. (6), the IENSF

$$S(Q_x, \omega) = \{ |\langle \Psi_0^s(x_s - \sqrt{2}x'_0) \Psi_0^a(x_a) | \exp(iQ_x x_1) | \Psi_0^s(x_2 - \sqrt{2}x'_0) \Psi_0^a(x_a) \rangle|^2 + |\langle \Psi_0^s(x_s - \sqrt{2}x'_0) \Psi_0^a(x_a) | \exp(iQ_x x_2) | \Psi_0^s(x_s - \sqrt{2}x'_0) \Psi_0^a(x_a) \rangle|^2 \} \delta(\omega) \quad (14)$$

gives

$$S(Q_x, \omega) = 2 \exp \left[-Q_x^2 \left(\frac{u_{0x}^2}{2\sqrt{1+4\lambda_x}} + \frac{u_{0x}^2}{2} \right) \right] \delta(\omega). \quad (15)$$

The Gaussian profile is analogous to Eq. (10). Practically, it is impossible to distinguish coupled pairs of bosons and isolated oscillators.

D. Pair of coupled fermions

In KHCO_3 the spin-spin interaction for protons separated by $\sim 2 \text{ \AA}$ is on the order of 10^4 Hz while the exchange integral and tunnel splitting are negligible. In addition, there is no relaxation by phonons if the proton dynamics are decoupled from the lattice. Therefore, quantum coherence might survive on a rather long time scale ($\sim 10^{-4} \text{ s}$), if there is no further relaxation mechanisms. The neutron velocity ($\sim 10^4 \text{ ms}^{-1}$) and the coherence length ($\lambda^2/2\Delta\lambda \sim 20 \text{ \AA}$) are such that quantum coherence in the ground state is probed on a sufficiently short time scale ($\sim 10^{-12} \text{ s}$) to observing interferences.¹³

The singlet and triplet states are formally analogous to the para and ortho species of the hydrogen molecule.⁸ However, for a pair of indistinguishable fermion oscillators, the inter-

ference effects due to spin correlation combine with those due to indistinguishable particles: the scattering amplitude operator $\hat{b}_1(\hat{b}_2)$ can be at site 1 (2) or 2 (1). With the wave functions given in Eq. (7), the IENSF

$$S(Q_x, \omega) = | \langle \Theta_{0\pm} | \exp iQ_x(x_1 - x'_0) \pm \exp iQ_x(x_1 + x'_0) | \Theta_{0\pm} \rangle |^2 + | \langle \Theta_{0\pm} | \exp iQ_x(x_2 - x'_0) \pm \exp iQ_x(x_2 + x'_0) | \Theta_{0\pm} \rangle |^2 \delta(\omega) \quad (16)$$

gives

$$S(Q_x, \omega)_{0+0+} = 2 \cos^2(Q_x x'_0) \left[\cos(Q_x x'_0) + \exp \left(-\frac{x_0'^2}{2u_{0x}^2} \right) \right]^2 \times \exp \left[-Q_x^2 \left(\frac{u_{0x}^2}{2\sqrt{1+4\lambda_x}} + \frac{u_{0x}^2}{2} \right) \right] \delta(\omega),$$

$$S(Q_x, \omega)_{0+0-} = S(Q_x, \omega)_{0-0+} = 2 \sin^4(Q_x x'_0) \times \exp \left[-Q_x^2 \left(\frac{u_{0x}^2}{2\sqrt{1+4\lambda_x}} + \frac{u_{0x}^2}{2} \right) \right] \delta(\omega),$$

$$S(Q_x, \omega)_{0-0-} = 2 \cos^2(Q_x x'_0) \left[\cos(Q_x x'_0) - \exp \left(-\frac{x_0'^2}{2u_{0x}^2} \right) \right]^2 \times \exp \left[-Q_x^2 \left(\frac{u_{0x}^2}{2\sqrt{1+4\lambda_x}} + \frac{u_{0x}^2}{2} \right) \right] \delta(\omega). \quad (17)$$

The Gaussian profile, analogous to Eq. (15) for bosons, is modulated by $\sin^4(Q_x x'_0)$ and $\cos^4(Q_x x'_0)$ factors. The exponential terms are negligible for $x_0'^2/2u_{0x}^2 \gg 1$. In contrast to the double minimum potential, the interference pattern can be observed for the degenerate ground state with maxima of intensity at $Q_x x'_0 = n\pi$ for $S(Q_x, \omega)_{0+0+}$ or $S(Q_x, \omega)_{0-0-}$ and at $Q_x x'_0 = (n+1/2)\pi$ for $S(Q_x, \omega)_{0+0-}$ or $S(Q_x, \omega)_{0-0+}$ (see Fig. 6, curve 3).

The best fits to cuts of $S(Q_x, Q_y, 0)$ and $S(Q_x, Q_z, 0)$ along $\nu \text{ OH}$, $\delta \text{ OH}$, and $\gamma \text{ OH}$ modes, obtained with Eq. (17) are presented in Figs. 9–12. The mean-square amplitudes, very similar to those derived previously with Eq. (10) (see Table II), are largely model independent. However, the number of triangular functions is less with Eq. (17). Only the Bragg-like peaks at large momentum transfer ($> 15 \text{ \AA}^{-1}$) are not accounted for. The peaks at low $|\mathbf{Q}|$ values ($< 3 \text{ \AA}^{-1}$) may be due to multiple-scattering contributions more probable in this $|\mathbf{Q}|$ range.

Quantum interferences account for maxima of intensity observed at $\sim \pm 5 \text{ \AA}^{-1}$, which are maxima of $S(Q, \omega)_{0+0-}$ or $S(Q, \omega)_{0-0+}$, and for weaker shoulders at $\sim \pm 10 \text{ \AA}^{-1}$,

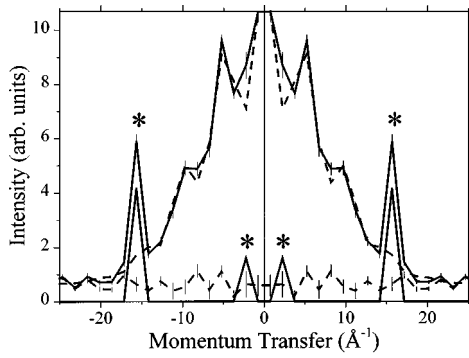


FIG. 9. KHCO_3 : cut of $S(Q_x, Q_y, 0)$ at $\pm 20^\circ$ with respect to Q_x . Comparison of the measured profile (solid line with error bars) to the best fit (dash line) obtained with Eq. (17) and four triangular functions (solid line and *) attributed to other scattering processes. $u_{0x}^2 = 0.94 \times 10^{-2} \text{ \AA}^2$ ($\hbar\omega_{0x} = 1780 \text{ cm}^{-1}$); $x'_0 = 0.31 \text{ \AA}$. The dash line with error bars is the difference spectrum.

which are secondary maxima of $S(Q, \omega)_{0+0+}$ or $S(Q, \omega)_{0-0-}$. These features occur for virtually all Q directions (see Figs. 2 and 3). They cannot be confused with Bragg-like reflections.

E. Discussion

1. Quantum interferences

The x'_0 , y'_0 and z'_0 values of $\sim 0.3 \text{ \AA}$ derived from the experiments (r_0 in Table II) do not correspond to distances between proton sites in the crystal structure. The shortest distance between protons is $\sim 2.25 \text{ \AA}$ within a dimer and protons in different dimers are much further away. Alternatively, the distances between projections of the proton positions onto Q_x , Q_y , and Q_z are close to $2x'_0$, $2y'_0$, and $2z'_0$, respectively. Along Q_x , $2x'_0$ is the distance between the two proton sites of a dimer. Along Q_y , $2y'_0$ is the shortest distance between the projections of protons belonging to adjacent dimers (for example, those labeled 1 and 2 in Fig. 1). The great similarity of $2x'_0$ and $2y'_0$ is in accord with the crystal structure as the b unit-cell parameter ($\sim 5.6 \text{ \AA}$) is twice the size of a dimer along the same direction ($\sim 2.25 \text{ \AA}$)

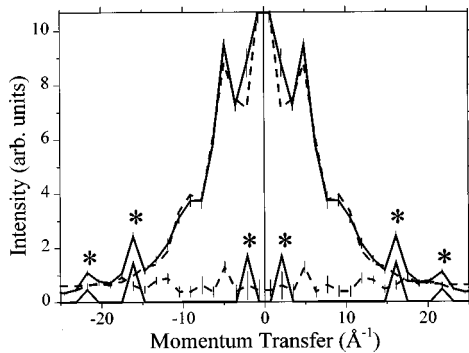


FIG. 10. KHCO_3 : cut of $S(Q_x, Q_y, 0)$ along Q_y . Comparison of the measured profile (solid line with error bars) to the best fit (dash line) obtained with Eq. (17) and six triangular functions (solid line and *) attributed to other scattering processes. $u_{0y}^2 = 1.26 \times 10^{-2} \text{ \AA}^2$ ($\hbar\omega_{0y} = 1325 \text{ cm}^{-1}$); $y'_0 = 0.31 \text{ \AA}$. The dash line with error bars is the difference spectrum.

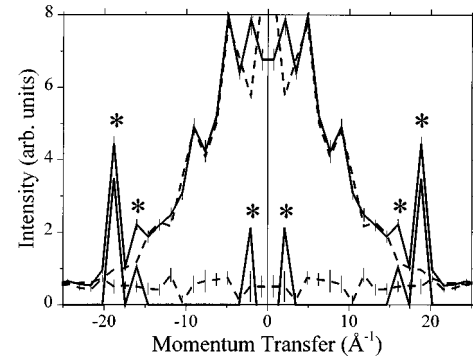


FIG. 11. KHCO_3 : cut of $S(Q_x, Q_z, 0)$ along Q_x . Comparison of the measured profile (solid line with error bars) to the best fit (dash line) obtained with Eq. (17) and six triangular functions (solid line and *) attributed to other scattering processes. $u_{0x}^2 = 0.84 \times 10^{-2} \text{ \AA}^2$ ($\hbar\omega_{0x} = 2000 \text{ cm}^{-1}$); $x'_0 = 0.33 \text{ \AA}$. The dash line with error bars is the difference spectrum.

plus twice $\sim 2y'_0$.²² Along Q_z , interferences arise because protons are located out of the middimer plane. With an OH bond length (l) of $\sim 1 \text{ \AA}$,²² the estimated value for $z'_0 = l \sin \theta$ gives a deviation (θ) of $\pm 14^\circ$. Therefore, the OH bonds should be almost parallel to the (a, b) crystal plane.

The quantum interferences reveal that proton spins are correlated in the (103) plane, should they belong or not to the same dimer entity. The spin correlation is observed for rather large distances in real space. The r_0 values indicate that neutrons are scattered coherently by lines of protons parallel to the (103) planes.

2. The proton dynamics

The mean-square amplitudes given in Table II are virtually model independent and close to those anticipated for isolated proton oscillators. Systematic deviations arise because the momentum transfer directions Q_x , Q_y , and Q_z are not exactly parallel to the proton modes. This is an unavoidable consequence of the crystal structure (Fig. 1). The dynamics along Q_x include minor contributions of the bending modes which increase u_{0x}^2 , while u_{0z}^2 is diminished by contributions of the stretching mode. For u_{0y}^2 the stretching and

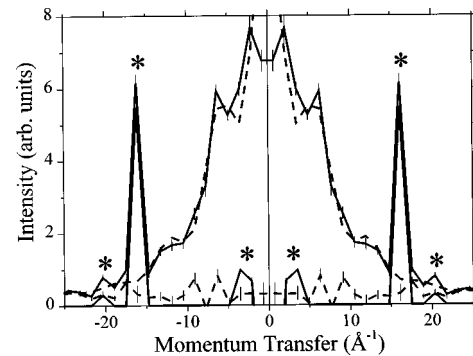


FIG. 12. KHCO_3 : cut of $S(Q_x, Q_z, 0)$ along Q_z . Comparison of the measured profile (solid line with error bars) to the best fit (dash line) obtained with Eq. (17) and six triangular functions (solid line and *) attributed to other scattering processes. $u_{0z}^2 = 1.36 \times 10^{-2} \text{ \AA}^2$ ($\hbar\omega_{0z} = 1230 \text{ cm}^{-1}$); $z'_0 = 0.24 \text{ \AA}$. The dash line with error bars is the difference spectrum.

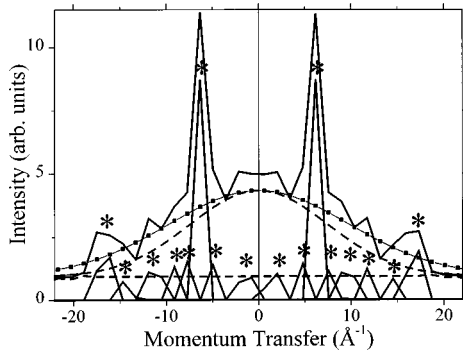


FIG. 13. KDCO₃: cut of $S(Q_x, Q_z, 0)$ along Q_x . Comparison of the measured profile (solid line with invisible error bars) to the best fit (dash line) obtained with a harmonic profile ($u_{0x}^2 = 0.91 \times 10^{-2} \text{ \AA}^2$, $\hbar\omega_{0x} = 920 \text{ cm}^{-1}$) and 16 triangular functions (solid line and *) attributed to other scattering processes. (—■—): calculated as the sum of two Gaussian profiles with $U_{0x}^2 = 0.5 \times 10^{-2} \text{ \AA}^2$ (70%) and $u_{0xD}^2 = 0.58 \times 10^{-2} \text{ \AA}^2$ (30%), respectively.

out-of-plane bending modes have opposite contributions. Fortunately, the deviation of the OH bond from the ideal orientation is no more than 20° and the contamination by other modes is less than 10%.

For the stretching mode, u_{0x}^2 derived from $S(Q_x, Q_y, 0)$ is in accord with the double minimum potential function.^{25–27} A numerical calculation of the wave function gives the same value. This remarkable agreement confirms that multiple-scattering and/or crystal misalignment effects are negligible. (Both they should diminish u_{0x}^2). The smaller amplitude derived from $S(Q_x, Q_z, 0)$ could reflect the large anisotropy of the double minimum potential since the momentum transfer is along the long dimer axis for $S(Q_x, Q_z, 0)$, or along the OH bond direction for $S(Q_x, Q_y, 0)$.

For the in-plane bending mode, u_{0y}^2 is slightly greater than anticipated from the vibrational frequency at $1385\text{--}1440 \text{ cm}^{-1}$.¹⁰ The discrepancy of $\sim 5\%$ is representative of the accuracy of the measurements. Anharmonicity is unlikely to increase u_{0y}^2 .

For the out-of-plane bending mode, $u_{0z}^2 = (1.75 \pm 0.02)10^{-2} \text{ \AA}^2$ is smaller than anticipated for a harmonic oscillator. However, such a large anharmonicity is not confirmed by the vibrational spectra.^{25–27} Some contribution of the stretching mode is likely.

The mean-square amplitudes for the O atoms derived from x-ray diffraction at 95 K are $U_{0xO}^2 \sim U_{0yO}^2 \sim 0.5 \times 10^{-2} \text{ \AA}^2$ and $U_{0zO}^2 \sim 2.2 \times 10^{-2} \text{ \AA}^2$.²² If the protons were riding the O atoms, the observed mean-square amplitudes should be $u_{0i}^2 = u_{0iH}^2 + U_{0iO}^2$, with $i = x, y$ or z ($\sim 1.4, 1.75$, and 3.5 in 10^{-2} \AA^2 units, respectively). The observed profiles are too broad to be amenable to protons riding O atoms.

The proton dynamics in the ground state were previously measured with the neutron Compton scattering (NCS) technique which probes the mean kinetic momentum $\langle p_0^2 \rangle$.²¹ For an isolated harmonic oscillator $\langle p_0^2 \rangle \langle u_0^2 \rangle = 1/4$ with $\langle p_0^2 \rangle$ and $\langle u_0^2 \rangle$ in \AA^{-2} and \AA^2 units, respectively. For the stretching and out-of-plane bending modes the NCS and IENS measurements give $\langle p_{0x}^2 \rangle \langle u_{0x}^2 \rangle = 0.250$ and $\langle p_{0z}^2 \rangle \langle u_{0z}^2 \rangle = 0.233$, re-

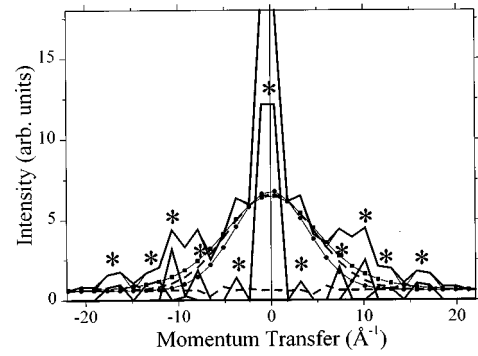


FIG. 14. KDCO₃: cut of $S(Q_x, Q_z, 0)$ along Q_z . Comparison of the measured profile (solid line with invisible error bars) to the best fit (dash line) obtained with a harmonic profile ($u_{0z}^2 = 2.31 \times 10^{-2} \text{ \AA}^2$, $\hbar\omega_{0z} = 360 \text{ cm}^{-1}$) and 11 triangular functions (solid line and *) attributed to other scattering processes. (—■—): calculated as the sum of two Gaussian profiles with $U_{0z}^2 = 2.5 \times 10^{-2} \text{ \AA}^2$ (70%) and $u_{0zD}^2 = 0.92 \times 10^{-2} \text{ \AA}^2$ (30%), respectively. (—●—): Gaussian profile calculated with $u_{0z}^2 = 3.4 \times 10^{-2} \text{ \AA}^2$.

spectively. The proton dynamics are thus amenable to harmonic oscillators within $\sim 10\%$ accuracy. This is another confirmation that multiple-scattering effects, which should decrease $\langle p_0^2 \rangle$ and/or $\langle u_0^2 \rangle$, were negligible for both techniques, and that the proton dynamics in the ground state are largely decoupled from the lattice.³¹

The harmonic character of the stretching mode ground state is not in conflict with the large anharmonicity of the asymmetric double-well potential derived from vibrational spectra. It merely confirms that the proton delocalization in the ground state (tunneling) is negligible.

The proton mean-square amplitudes obtained in previous neutron diffraction works at 298 K,²³ $(2.8224 \pm 0.0004)10^{-2}$, $(3.0276 \pm 0.0004)10^{-2}$, and $(5.1076 \pm 0.0004)10^{-2} \text{ \AA}^2$, are greater by a factor of $\sim 3\text{--}4$ than those obtained from IENS measurements (Table II). They are even much greater than anticipated if the protons were coupled to the lattice. Presumably, the mean-square amplitudes should be substantially reduced for diffraction experiments performed at low temperature.

3. The deuteron dynamics

For KDCO₃, coherent and incoherent scattering cannot be distinguished easily (Fig. 4). Nevertheless, cuts along Q_x and Q_z can be decomposed into Gaussian profiles and triangular functions (Figs. 13, 14 and Table II). Owing to the large number of triangular functions, the decomposition could be not unique and the uncertainties given in Table II are certainly underestimated. There is no evidence for quantum interferences similar to those observed for the hydrogenated analog. However, this is not conclusive because of the many Bragg-like peaks.

The most significant information is provided by the width of the Gaussian profiles that comprise incoherent scattering, mainly by D atoms, and unresolved coherent scattering by D, O, and C atoms (Table I). The relative contributions of the D, C, and O atoms to the total intensity are $\sim 30\%$ (D), 20% (C), and 50% (O).

The mean-square amplitudes for the O and C atoms derived from x-ray diffraction at 95 K are similar: $U_{0x}^2 \sim$

- ¹⁸J. L. Skinner and H. P. Trommsdorff, *J. Chem. Phys.* **89**, 897 (1988).
- ¹⁹A. J. Horsewill and A. Aibout, *J. Phys.: Condens. Matter* **1**, 9609 (1989); A. Stäckli, B. H. Meier, R. Kreis, R. Meyer, and R. R. Ernst, *J. Chem. Phys.* **93**, 1502 (1990); A. Heuer and U. J. Haerberlen, *ibid.* **95**, 4201 (1991); A. J. Horsewill, A. Heidemann, and S. Hayashi, *Z. Phys. B* **90**, 319 (1993); A. J. Horsewill and A. Ikram, *Physica B* **226**, 202 (1996).
- ²⁰F. Fillaux, *Chem. Phys.* **74**, 405 (1983).
- ²¹P. Postorino, F. Fillaux, J. Mayers, J. Tomkinson, and R. S. Holt, *J. Chem. Phys.* **94**, 4411 (1991).
- ²²J. O. Thomas, R. Tellegren, and I. Olovsson, *Acta Crystallogr., Sect. B: Struct. Crystallogr. Cryst. Chem.* **30**, 1155 (1974).
- ²³J. O. Thomas, R. Tellegren, and I. Olovsson, *Acta Crystallogr., Sect. B: Struct. Crystallogr. Cryst. Chem.* **30**, 2540 (1974).
- ²⁴A. Novak, *Struct. Bonding (Berlin)* **18**, 177 (1974).
- ²⁵A. Novak, P. Saumagne, and L. D. C. Bock, *J. Chim. Phys. Phys.-Chim. Biol.* **60**, 1385 (1963).
- ²⁶K. Nakamoto, Y. A. Sarma, and K. Ogoshi, *J. Chem. Phys.* **43**, 1177 (1965).
- ²⁷G. Lucazeau and A. Novak, *J. Raman Spectrosc.* **1**, 573 (1973).
- ²⁸F. Fillaux, A. Lautié, J. Tomkinson, and G. J. Kearley, *Chem. Phys.* **154**, 135 (1991); F. Fillaux and J. Tomkinson, *ibid.* **158**, 113 (1991); F. Fillaux and J. Tomkinson, *J. Mol. Struct.* **270**, 339 (1992).
- ²⁹M. Bée, *Quasielastic Neutron Scattering* (Adam Hilger, Bristol, 1988).
- ³⁰C. Cohen-Tannoudji, B. Diu, and F. Laloë, *Mécanique Quantique* (Hermann, Paris, 1977), Vol. I, p. 576.
- ³¹M. Warner, S. W. Lovesey, and J. Smith, *Z. Phys. B* **51**, 109 (1983).
- ³²A. Einstein, B. Podolsky, and N. Rosen, *Phys. Rev.* **47**, 777 (1935).